Modern Physics Letters B
Vol. 39, No. 14 (2025) 2450500 (16 pages)

DOI: 10.1142/S0217984924505006

World Scientific
www.worldscientific.com

Double formant PCF-SPR sensor with high sensitivity and wide detection range for detecting analytes with low refractive indexes

Xingdi Luo*, Wei Liu*, Xili Lu†, Jingwei Lv*, Lin Yang*, Qiang Liu*, Paul K. Chu‡ and Chao Liu*,§

*School of Physics and Electronic Engineering, Northeast Petroleum University, Daqing 163318, China

†School of Materials Science and Chemical Engineering, Harbin Engineering University, Harbin 150001, China

‡Department of Physics, Department of Materials Science and Engineering, and Department of Biomedical Engineering, City University of Hong Kong, Tat Chee Avenue, Kowloon, Hong Kong, China

§msm-liu@126.com

Received 18 April 2024
Revised 21 May 2024
Accepted 24 May 2024
Published 17 August 2024

A double U-shaped PCF-SPR sensor is proposed for the detection of analytes with low refractive indexes (RI). The U-shaped structure facilitates the penetration of analytes. Compared with a single formant sensor, the sensor exhibits double formant characteristics. Therefore, the analytes to be measured can be identified more accurately. This study employs the finite element method (FEM) to analyze the sensor. The findings suggest that the sensor is capable of detecting analytes with low RI ranging from 1.15 to 1.33 over an ultra-wide wavelength range of 800–6400 nm. The maximum wavelength sensitivities of the first and second peaks of the sensor are 54,300 nm/RIU and 60,000 nm/RIU, respectively. In addition, this paper introduces double peak shift sensitivity (DPSS), the highest DPSS value is 55,700 nm/RIU. Owing to these distinct characteristics, the sensor has great application prospects in the field of biosensing, especially in drug detection.

Keywords: Photonic crystal fiber; gold nanowires; surface plasmon resonance; low refractive index; double resonance.

1. Introduction

Surface plasmon resonance (SPR) is an important optical coupling phenomenon that arises from the oscillation of free electrons as they propagate between an evanescent

§Corresponding author.

wave (EW) and the metal–dielectric interface.[1] The sensors based on SPR technology possess a range of unique characteristics, including high precision, fast response, tag-free detection, high sensitivity, and dynamic monitoring.[2] Therefore, SPR sensors have great application potential in the field of biosensing. Such as the detection of trace elements in the blood, the identification of cancer cells in biological bodies, the detection of additives and pesticide residues in food, and the detection of drug elements.[3–8]

The SPR was theoretically discovered by Ritchie *et al.* in the 1950s,[9] and subsequently Kretschmann proposed a prism-coupled SPR sensor structure,[10] but it is large and bulky and not conducive to the miniaturization of the system.[11] SPR optical fiber sensors with small volume, simple structure and strong anti-interference ability have been proposed.[12] Conventional optical fiber sensors, including single-mode and multi-mode fibers, have solved some of the problems associated with prism sensors, such as large volume and complex structure, but poor mode coupling hinders their further development.[13,14] Compared to conventional fibers, photonic crystal fibers have many merits, such as flexible structures, high controllability and excellent mode coupling.[15] Additionally, high sensing performance can be easily achieved by varying the arrangement and size of the pores in the cladding.[16]

In recent years, although various high-performance PCF-SPR refractive index (RI) sensors have been reported, most of these sensors detect large RIs rather than small Ris.[17–19] For example, the PCF-SPR refractive index sensor designed by Z. Yin *et al.* is capable of detecting analytes with refractive indexes ranging from 1.35 RIU to 1.41 RIU, possessing a peak wavelength sensitivity of 8400 nm/RIU.[12] In another study, Hossaina *et al.* presented a biosensor with a peak wavelength sensitivity of 15,000 nm/RIU for refractive indexes between 1.42 RIU and 1.46 RIU.[11] Ahmed *et al.* also proposed a single-mode eccentric core D-type PCF-SPR refractive index sensor, achieving a remarkable sensitivity of 21,200 nm/RIU for refractive indexes spanning from 1.33 to 1.42 RIU.[16] However, many drugs have small refractive indexes (1.27–1.33),[20] and the design of PCF-SPR sensors capable of detecting small refractive indexes has important practical implications.

An important feature of the PCF-SPR sensor designed in this study is its double peak, which is rarely reported in PCF-SPR sensors. The dual resonance peak sensors reported so far are generally caused by the use of two plasma materials,[21,22] whereas in this paper, the proposed sensor uses only one plasma material, gold nanowires. The sensor has an ultra-wide operating wavelength range covering the near-infrared, mid-infrared and far-infrared bands, which leads to a splitting of the evanescent field[23] and hence a double resonance occurs, resulting in a double peak. This improves the accuracy of the detection of the analyte RI as it provides the opportunity to verify with another resonance peak. Furthermore, as the first and second peaks operate at different wavelength bands, it is possible to detect analytes using a single peak by controlling the range of operating wavelengths, in addition to using a double peak to detect the analyte.

The proposed sensor is capable of detecting analytes with refractive indices in the range of 1.15–1.33, especially in the range of 1.15–1.32, where the loss curve exhibits a double formation peak feature. In this paper, the sensing performance was analyzed using the wavelength interrogation method. The results show that the wavelength sensitivity (WS) of the first formation peak is 54300 nm/RIU, and the WS of the second formation peak is 60,000 nm/RIU. In addition, this paper not only investigates the displacement of single formation peaks, but also analyzes the double-peak displacement, and introduces the concept of double peak shift sensitivity (DPSS), and the maximal DPSS of this sensor is 55,700 nm/RIU. In view of these excellent sensing properties, the sensor has great potential for applications in biosensing, especially drug monitoring.

2. Structure and Principles

The two-dimensional cross-section of the proposed PCF-SPR sensor is shown in Fig. 1. The sensor's cladding is composed of 16 large air holes of diameter D_1, 4 small air holes of diameter D_2, and two U-shaped slots. The large air holes are arranged in a square pattern, while the small air holes are arranged in a straight line. With rational adjustment of the size and position of the large air holes, the dimensions of the fiber core can be altered, thus modifying the SPR effect. The small air holes break the symmetry of the fiber structure, thus changing the polarization state of the fiber to optimize the sensing performance of the Y polarization state. The U-shaped slot reduces the spacing between the sensing layer of the Au nanowires and the fiber core, enabling the sensor to respond to changes in the analyte RI near the sensing layer at a faster rate,[24,25] thus improving the sensing characteristics. The outermost green area in Fig. 1 is the perfect matching layer (PML) of the sensor, which absorbs all the radiation. Gold nanowires are placed in a double U-shaped slot to excite SPR, which replaces the conventional coating methodology and reduces the manufacturing complexity and difficulty.

The 3D PCF model of the sensor is shown in Fig. 2. The preparation technology of PCF has been quite mature.[26,27] For example, Wang *et al.* fabricated PCF with six

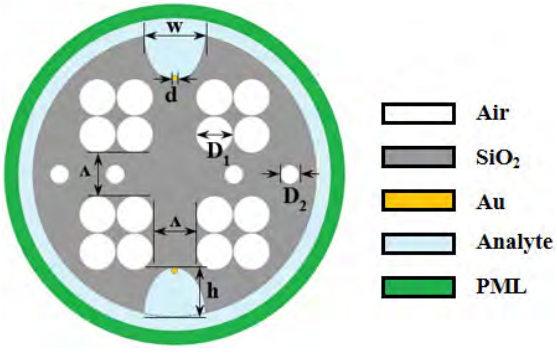

Fig. 1. (Color online) Two-dimensional cross-section of the sensor.

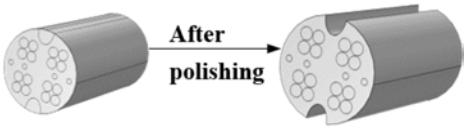

Fig. 2. 3D structure of the PCF.

air holes using brushed tala.[26] The PCF presented in this paper can be fabricated by stack-drawing and polishing processes, and the gold nanowires of the plasma sensing layer can be prepared by thermochemical vapor deposition and metal-organic vapor deposition.[28]

Au has been chosen as the plasmonic medium because of its stability and its excellent resistance to oxidation. The Drude–Lorentz model[11] can be used to represent the dielectric constant of Au as indicated by

$$\varepsilon_{\mathrm{Au}} = \varepsilon_{\infty} - \frac{\omega_p^2}{\omega(\omega + i\omega_D)} - \frac{\Delta\varepsilon \cdot \Omega_L^2}{(\omega^2 - \Omega_L^2) + i\Gamma_L\omega}. \tag{1}$$

Here, $\varepsilon_{\infty} = 5.9673$ is the dielectric constant at high frequencies. The weighting factor value is $\Delta\varepsilon = 1.09$ and ω is the angular frequency. Plasma frequency $\omega_p = 4227.2\pi\,\mathrm{THz}$, damping frequency $\omega_D = 31.84\pi\,\mathrm{THz}$, oscillator intensity $\Omega_L = 1300.14\pi\,\mathrm{THz}$, spectral width $\Gamma_L = 209.72\pi\,\mathrm{THz}$.

Molten silica serves as the primary material for the cladding region. The properties of fused quartz can be derived by the Sellmeier equation shown by[29]

$$n^2(\lambda) = 1 + \frac{\mathrm{M}_1\lambda^2}{\lambda^2 - N_1} + \frac{M_2\lambda^2}{\lambda^2 - N_2} + \frac{M_3\lambda^2}{\lambda^2 - N_3}, \tag{2}$$

where λ represents the input wavelength in μm, n stands for refractive index, M_1, M_2, M_3, N_1, N_2, and N_3 are 0.696163, 0.4079426, 0.897794, 0.004679148, 0.01351206 and $97.93400\,\mu\mathrm{m}^2$, respectively.

Evaluating the performance of PCF-SPR sensors necessitates considering the confined loss (CL), which serves as a crucial metric. The effective refractive index consists of both a real part $R[n_{\mathrm{eff}}]$ and an imaginary part $\mathrm{Im}[n_{\mathrm{eff}}]$. The attenuation of the light wave propagating in the medium is related to $\mathrm{Im}[n_{\mathrm{eff}}]$. The calculation of CL can be performed by[30]

$$\mathrm{CL} = 8.686 \times \frac{2\pi}{\lambda} \times \mathrm{Im}[n_{\mathrm{eff}}] \times 10^7\,(\mathrm{dB/cm}), \tag{3}$$

Here, λ is the incident wavelength in nm. According to Eq. (3), the CL at various wavelengths can be accurately computed.

3. Optimal Structural Parameter Investigation

Once the structure of the PCF-SPR sensor is determined, factors such as the thickness of the SPR material, the size and spacing of pores in the cladding, and the

polished area of the U-shaped opening ring can have a significant impact on the sensing characteristics of the sensor. In this paper, the influence of various structural parameters on the sensing characteristics is thoroughly investigated using the control variable method, and the optimal structural parameters are determined.

3.1. *Diameter of gold nanowires*

Figure 3(a) depicts the CL spectra for varying diameters (d) of gold nanowires. With increasing d, the first peak experiences a blueshift, the second peak undergoes a redshift, and the loss gradually decreases. The coupling strength between the plasmonic and basic modes weakens. When $d = 0.6\,\mu$m, the loss of double peaks is large, which is not conducive to long-distance transmission, and it has the largest full width at half maximum (FWHM), so its performance is poorer. When $d = 0.8\,\mu$m, the loss peak decreases, indicating that resonance between the basic and plasmonic modes weakens. By considering the overall situation, d is selected to be $0.7\,\mu$m.

3.2. *Diameter and spacing of air holes*

The CL curves of large air holes with different diameters (D_1) are plotted in Fig. 3(b). As D_1 increases from $3.8\,\mu$m to $4.2\,\mu$m, the loss peak gradually increases, but the change is not significant. When D_1 is too large, the narrow gap between the holes and the outer wall of the fiber cladding significantly increases the manufacturing difficulty. If D_1 is excessively small, the capacity of the large pores to confine light diminishes, evident in the electric field diagram as significant light leakage. Consequently, $4.0\,\mu$m is chosen as the optimal value for D_1. As depicted in Fig. 3(c), the RW and CL values associated with the double peak remain virtually unchanged as the diameter (D_2) of the smaller air holes varies within the range of 1.6–$2.4\,\mu$m. Nevertheless, additional computation indicates that when $D_2 = 2\,\mu$m, sensing characteristics such as wavelength sensitivity and resolution are improved. Figure 3(d) depicts the loss spectra for different pore spacings (Λ). With increasing Λ, the first peak blueshifts and the second peak redshifts. The loss diminishes gradually, but the change is not obvious. When Λ is excessively small, the fiber core will experience compression in both the horizontal and vertical directions, resulting in a reduced core size and increased energy concentration inside the core. Consequently, more energy will be transported from the core to the sensing layer, leading to a rise in CL. The manufacturing of the sensor becomes more challenging if the spacing between the pores is excessively great, as this shortens the spacing between the pores and the fiber's outer wall. After our comprehensive consideration, $5.0\,\mu$m is the optimal value for Λ.

3.3. *U-shaped depth and width*

Figures 3(e) and 3(f) present the fundamental mode loss spectra for different U-shaped depths (h) and widths (w), respectively. As h increases, the first peak

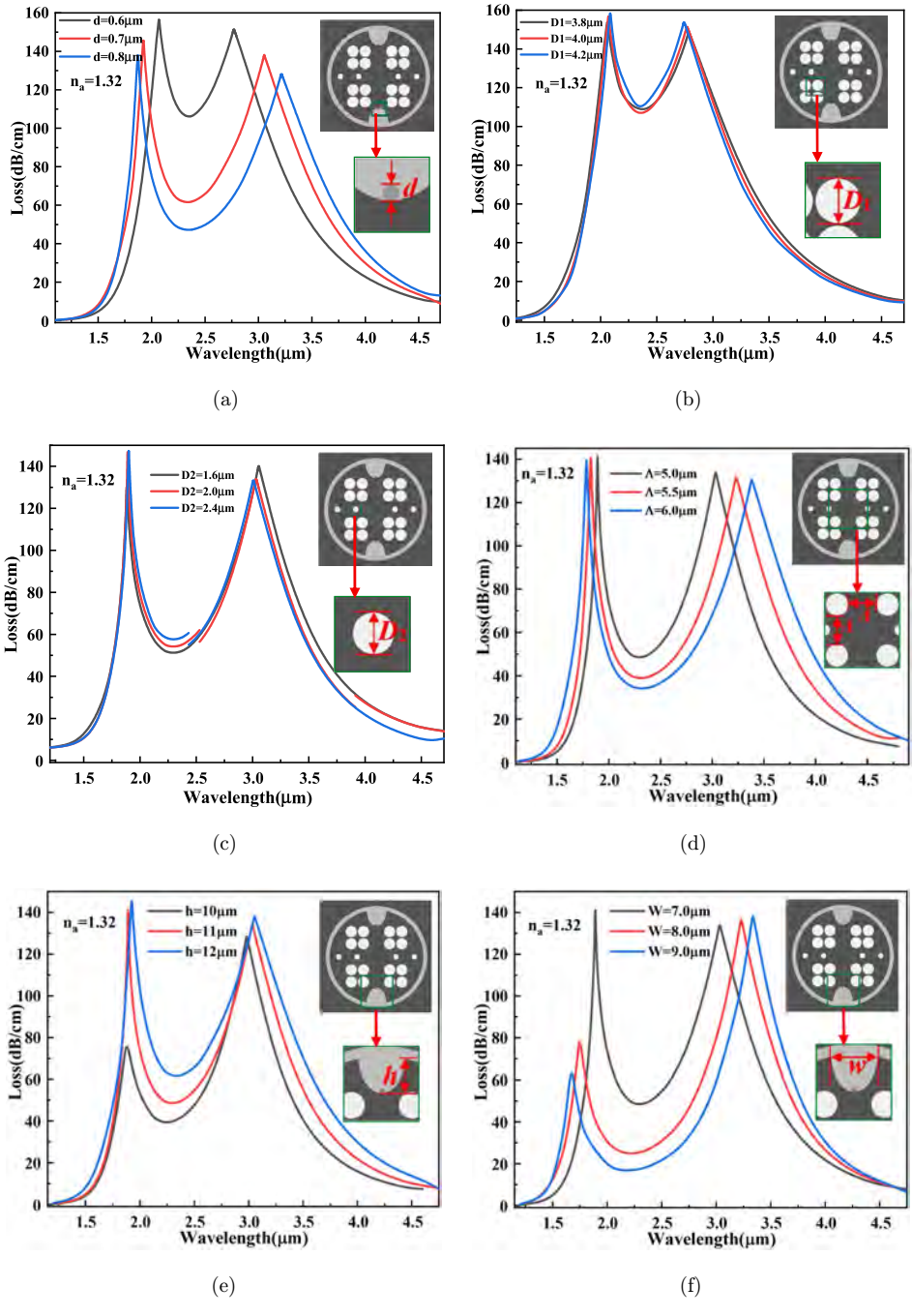

Fig. 3. (Color online) Dependence of CL on wavelengths: (a) d, (b) D_1, (c) D_2, (d) Λ, (e) h and (f) w ($n_a = 1.32$).

redshifts and the second peak blueshifts. When h increases from 10 μm to 11 μm, the first peak rises sharply and becomes very sharp, indicating that the coupling effect between the plasma and the fundamental modes is better. When h goes up from 11 μm to 12 μm, the loss and RW of the double peaks do not change significantly. A bigger polishing depth increases the manufacturing difficulty. Hence, h is selected to be 11 μm. With increasing w, the loss of the first peak decreases sharply and then slightly, and the second peak loss changes slightly. Therefore, here we only consider the effect of w change on the sensing characteristics of the first peak. When $w = 7.0\,\mu$m, the first peak loss is the largest and very sharp, at this moment, the plasma mode absorbs the most energy from the fundamental mode, indicating a stronger mode coupling effect. Hence, SPR works better and w is determined to be 7.0 μm.

3.4. *Double resonance and polarization states*

The principle of coupling between the fundamental and plasmonic modes is illustrated in Fig. 4. Specifically, the intersection of the black solid line representing the $R[n_{\text{eff}}]$ of the fundamental mode and the blue solid line representing the $R[n_{\text{eff}}]$ of the SPP mode occurs at 1.565 μm and 3.680 μm, the loss spectrum represented by the red dashed line produces resonance peaks at these two intersection points, as seen in Fig. 4(A), which shows that the phase matching criterion is met. When the wavelength $\lambda < 1.565\,\mu$m, the solid blue line is above the solid black line, indicating that the energy of the SPP mode is higher than that of the fundamental mode. When the wavelength $\lambda = 1.565\,\mu$m, the propagation constant of the evanescing wave (EW) is equal to the propagation constant of the surface plasma wave (SPW) of the gold nanowires. The fundamental mode photon energy is continually absorbed by SPW as a result of the collective oscillation of free electrons on the metal surface, significantly

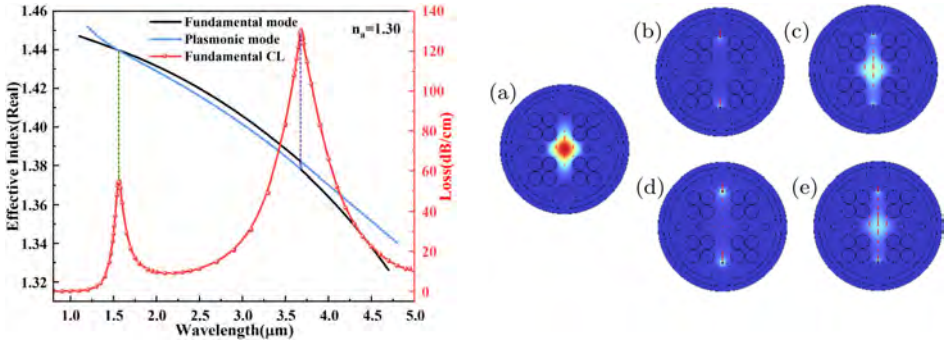

(A) (B)

Fig. 4. (Color online) Mode coupling principle: (A) Curve and (B) Electric field distribution: (a) Fundamental mode, (b) SPP mode of the first peak, (c) Resonance mode of the first peak, (d) SPP mode of the second peak, and (e) Resonance mode of the second peak ($n_a = 1.30$).

boosting the energy of SPP mode.[31] When the wavelength falls between 1.565 μm and 3.680 μm, photons shift to the fundamental mode, which lowers the energy of the SPP mode. When the wavelength $\lambda > 3.680\,\mu$m, the blue line is above the black line, which means that the energy of the SPP mode once again becomes higher compared to the fundamental mode. This leads to the double peak nature of this sensor and is also the reason for the redshift of the first formant and blueshift of the second formant.

Figure 4(B) shows the electric field distribution diagram of the sensor, in which (a) is the fundamental mode at the nonresonant wavelength, (b) and (d) show the SPP patterns near the first and second peaks, (c) and (e) show the resonant modes of the first and second peaks at the resonant wavelengths, respectively. It is not difficult to see that energy can be stably transmitted in the photonic crystal fiber.

As the structure is designed asymmetrically, the sensor has X-pol and Y-pol states. The CL curve and WS of the two polarization states are shown in Figs. 5(a)–5(c).

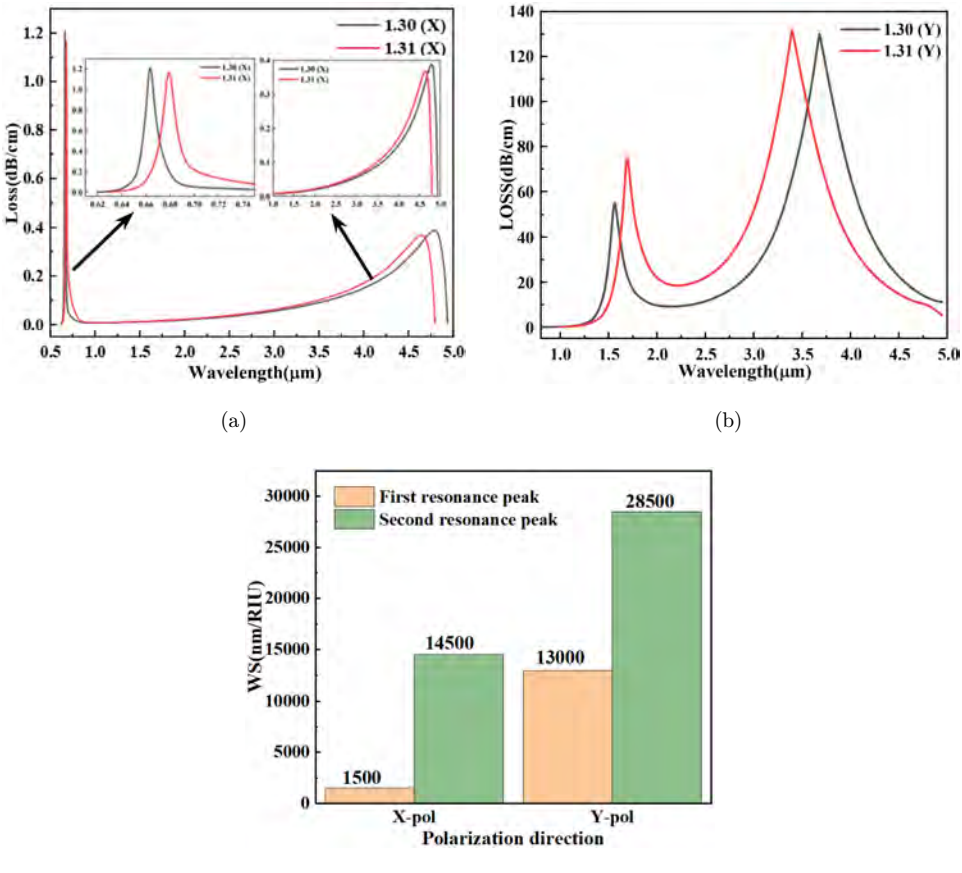

Fig. 5. (Color online) (a) X-pol CL, (b) Y-pol CL and (c) X-pol and Y-pol WS.

Both states display bimodal characteristics, with the sensitivity of the second formant being greater than the first. Furthermore, it can be observed that the sensitivity and loss of Y-pol are higher than those of X-pol, suggesting that Y-pol modes exhibit superior coupling, and the double peaks in the Y-pol are obvious and stable. Here, Y-pol is chosen for the subsequent analysis.

4. Results and Discussion

4.1. *Refractive index (RI) detection range*

The sensor can operate in the ultra-wide wavelength range between 800 nm and 6,400 nm, and within this spectral range, the sensor is capable of detecting analytes with refractive indexes (RI) spanning from 1.15 RIU to 1.33 RIU. The CL is calculated by Eq. (3). The variation of the CL spectra for different RIs with wavelength is illustrated in Fig. 6(a). Figures 6(b) and 6(c) show the CL spectra of the first formant and the second formant, respectively. With the gradual increase of analyte RI, the CL

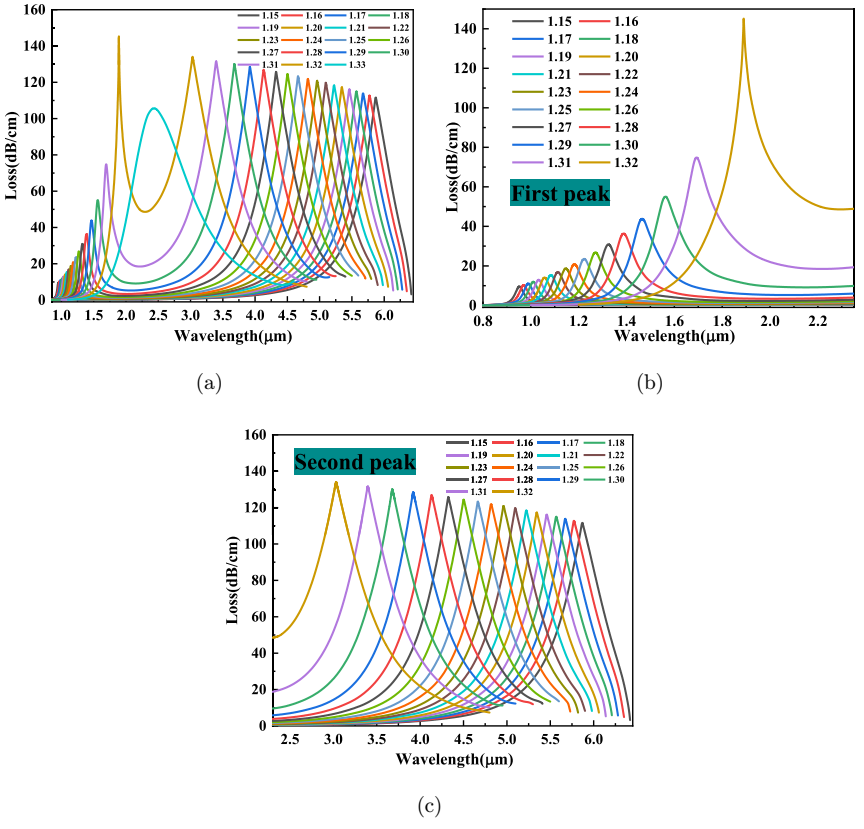

Fig. 6. (Color online) Dependence of CL on the wavelength at different RI. (a) Double peak CL spectra, (b) CL spectra of the first peak and (c) CL spectra of the second peak.

showed an upward trend. The RW of the first peak redshifts with increasing RI, and the RW of the second peak blueshifts with increasing RI. When the refractive index increases to 1.33, the two peaks merge into one peak. In the RI range of 1.15–1.32, since the resonance occurs twice, it provides the opportunity to verify using another resonance peak, which improves the accuracy of detecting the RI of the analyte. In addition, since the first and second peaks operate at different wavelength ranges, a single peak can be selected for RI detection by controlling the operating wavelength range.

4.2. *Maximum wavelength sensitivity and resolution*

The wavelength sensitivity (WS) is an important performance indicator of SPR sensors. The higher the WS, the more sensitive the sensor is to changes in the RI of the analyte. The WS is calculated according to the following equation:[32]

$$S_\lambda = \frac{\Delta\lambda_{\text{peak}}}{\Delta n_a}. \tag{4}$$

The difference in resonant wavelengths and refractive indexes is expressed in terms of $\Delta\lambda_{\text{peak}}$ and Δn_a, respectively. Figure 7(a) shows WS for different RI of the first peak and second peak of the sensor. As can be seen from the figure, as the RI rises, the WS

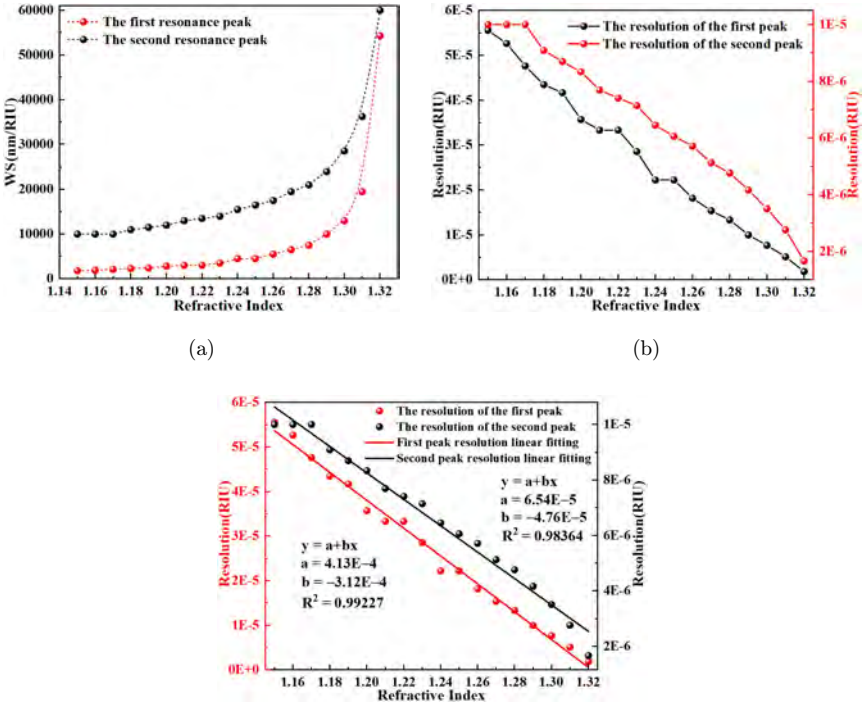

Fig. 7. (Color online) (a) WS of two peaks, (b) R of two peaks and (c) linear fitting of two peaks.

of the two formants also increases. The maximum WS of the first resonant peak is 54,300 nm/RIU, with an average WS of 8,227.778 nm/RIU. For the second resonant peak, the minimum WS exceeds 10,000 nm/RIU, with an average WS of 19,094.444 nm/RIU, and the maximum WS reaching 60,000 nm/RIU. While both peaks deliver good performance in detecting the RI of analytes, the second peak is better than the first.

The resolution (R) can reflect the degree of sensitivity of the SPR sensor to subtle variations in RI; the smaller the resolution, the better the sensing performance. R can be determined using the following equation[33,34]:

$$R = \frac{\Delta n_a \times \Delta\lambda_{\min}}{\Delta\lambda_{\text{peak}}} = \frac{\Delta\lambda_{\min}}{S_\lambda}(\text{RIU}). \tag{5}$$

The minimum detectable wavelength difference $\Delta\lambda_{\min}$ is typically instrument-dependent. In this case, it has been set to 0.1 nm to align with the spectrometer's specifications. Δn_a is the RI difference of the analyte, $\Delta\lambda_{\text{peak}}$ is the resonance wavelength difference, and S_λ is the wavelength sensitivity.

Figures 7(b) and 7(c) show the resolution curves and linear fitting of the two formant peaks, respectively. The expression for R is depicted in Fig. 7(c). With increasing RI, the R of the two formant peaks decreases gradually. The minimum R of the first formant and second formant is 1.842×10^{-6} RIU and 1.667×10^{-6} RIU, respectively.

4.3. *Resonance wavelength and sensing length*

The higher the linearity of the sensor's resonant wavelength (RW), the easier it becomes to predict the RW under different analyte refractive indices.[35] Figure 8(a) illustrates the RW of the first formant and the linear fit. Figure 8(b) plots the RW of the second formant and the linear fit. The linear fitting equations of bimodal RW are shown in Figs. 8(a) and 8(b). The first formant regression coefficient is $R^2 = 0.99687$ and the second formant $R^2 = 0.99959$, both of which are close to 1.

The sensor length (SL) can be calculated from the following equation,[31] and it is evident from the equation that a smaller loss results in a larger SL.

$$\text{SL} = \frac{1}{\alpha(\lambda, n_a)}(\text{cm}), \tag{6}$$

where the analyte loss is represented by $\alpha(\lambda, n_a)$. The link between SL and the analyte's RI is displayed, as seen in Figs. 8(a) and 8(b). As the RI rises, SL progressively falls, as the figures demonstrate. The maximum SL is 0.10428 cm, indicating that the sensor is conducive to long-distance sensing.

4.4. *Figure of merit*

The figure of merit (FOM), a crucial metric reflecting the sensor's quality, is calculated by dividing the WS by the full-width at half-maximum (FWHM), as shown

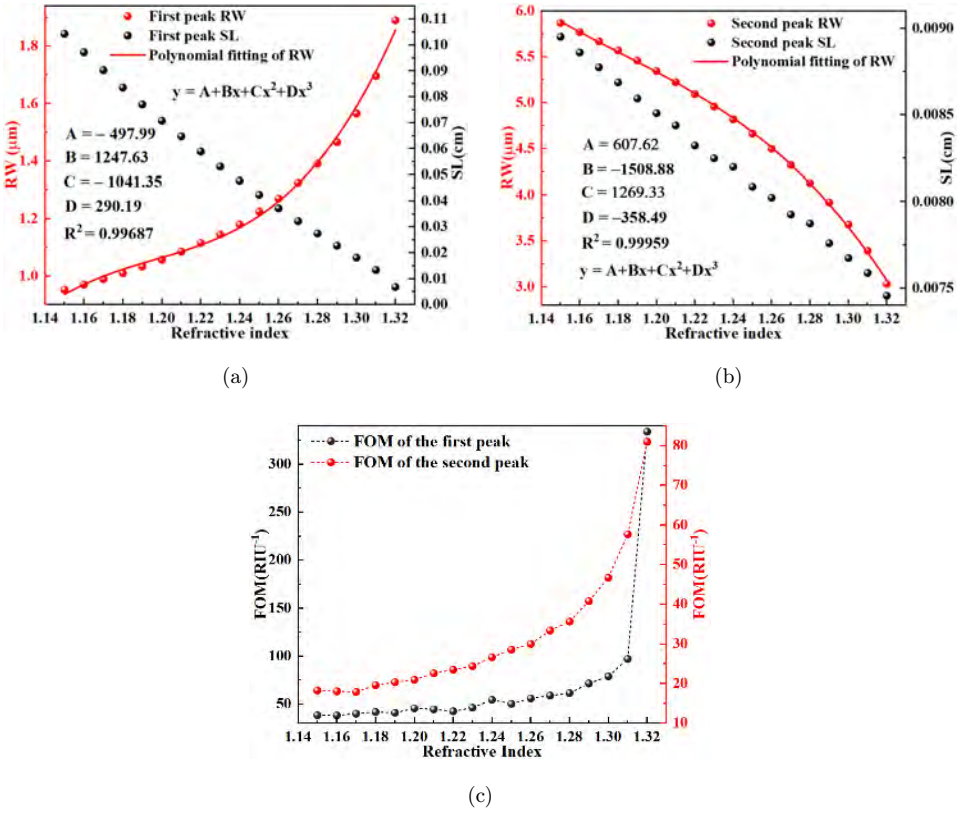

Fig. 8. (Color online) (a) RW and SL of the first peak, (b) RW and SL of the second peak and (c) FOM of the first and second peaks.

in the following equation[13]:

$$\mathrm{FOM} = \frac{S_\lambda}{\mathrm{FWHM}}(\mathrm{RIU}^{-1}). \tag{7}$$

Essentially, a higher FOM translates to superior overall sensor performance. Figure 8 (c) shows the FOM values of the two peaks and variations, which indicates that the FOM values of the two formants are positively correlated with the RI. When $n_a = 1.32$, both the first and second formants exhibit the maximum FOM of 333.744 RIU^{-1} and 80.960 RIU^{-1}, respectively, indicating that the detection accuracy of the first peak is higher.

4.5. *Double peak shift sensitivity*

Within the range of 1.15–1.32 RIU, the sensor produces two resonance peaks on the same spectrum. Observing Fig. 9(a), it is evident that as the RI increases, the RW difference between the two peaks diminishes, which is attributed to the redshift of the

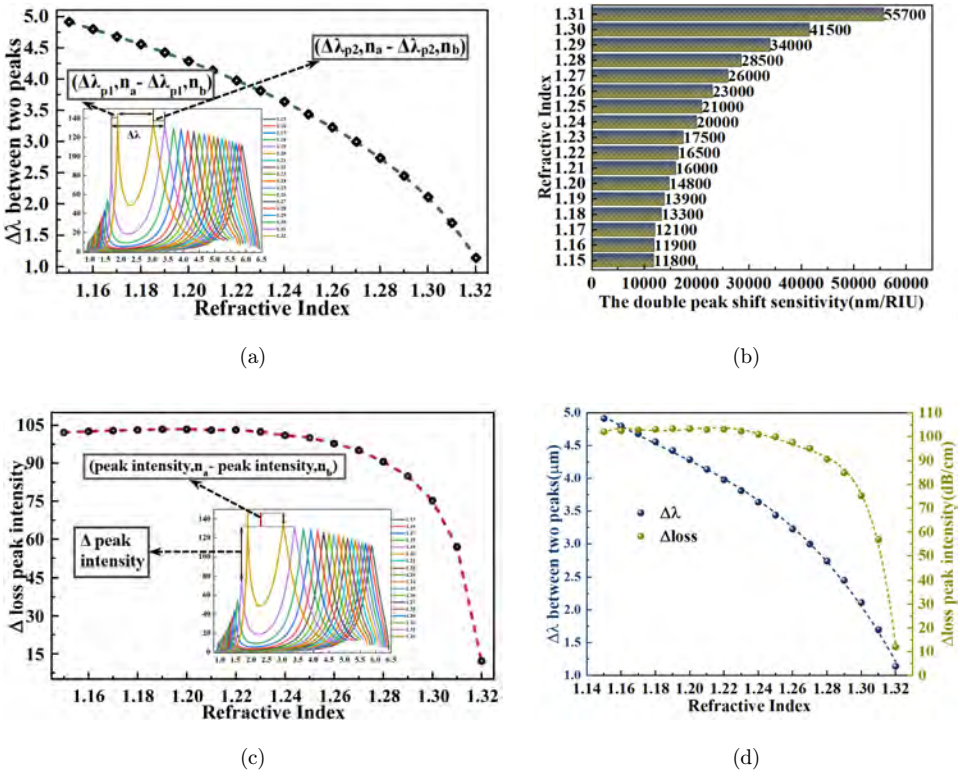

Fig. 9. (Color online) (a) RW difference, (b) DPSS, (c) CL difference and (d) linear fitting of CL difference and RW difference.

first formant and the blueshift of the second formant. In addition, the double-peak displacement sensitivity (DPSS) was introduced by extending the relationship between the distance between the two forming peaks and the RI. It can be calculated by Eq. (8).[21] A higher DPSS value corresponds to superior sensing properties.

$$S_{P-P} = \frac{(\lambda_{P2,n_a} - \lambda_{P2,n_b}) - (\lambda_{P1,n_a} - \lambda_{P1,n_b})}{n_b - n_a} \times 10^3 \,(\text{nm/RIU}), \tag{8}$$

where $\lambda_{P1,na}$ and $\lambda_{P1,nb}$ are the first resonant wavelengths of refractive indexes n_a and n_b, respectively, and $\lambda_{P2,na}$ and $\lambda_{P2,nb}$ are the resonant wavelengths of the second peak in μm. The DPSS of the sensor is all higher than 11,800 nm/RIU, with maximum and average DPSS of 55,700 nm/RIU and 22,206 nm/RIU, respectively. They are better than those in the literature.[21,36] The DPSS for different RIs is shown in Fig. 9(b).

According to the double formant loss spectra, it is evident that for the same analyte RI, the losses of the two formants are different. This is because, despite the same RI of the analyte, the maximum energy absorbed by the SPP mode from the

fundamental mode is not equal at different resonance wavelengths due to light scattering. Figure 9(c) depicts the relationship between the loss difference of the two formants and the RI for the same analyte RI. As the RI varies from 1.15 to 1.32, the loss difference between the two formants gradually decreases. During this process, the loss of the first formant increases slightly and then increases significantly, while the loss of the second formant remains almost unchanged. This unique property can distinguish analytes with different RIs.

Figure 9(d) displays the linear fits of the double peak RW difference and loss difference versus analyte RI. The maximum RW difference is 4.918 μm, and the maximum loss difference is 103.384 dB/cm. The regression coefficients R^2 of the RW difference and loss difference of the twin peaks are 0.99917 and 0.99844, respectively, indicative of high linearity, which is of great help in analyzing the sensing properties of the sensor.

5. Conclusion

In this paper, a PCF-SPR RI sensor with double polished U-shaped openings is proposed to excite SPR by placing gold nanowires inside the U-shaped openings. The sensor is capable of detecting analytes with RI in the range of 1.15–1.33. The loss spectra when the RI is in the range of 1.15–1.32 exhibit bimodal characteristics, with the first peak redshifted in the 800–2250 nm band and the second peak in the 2250–6400 nm band blueshifted. The wavelength sensitivities of the first and second peaks were as high as 54300 nm/RIU and 60000 nm/RIU, respectively, and the optimal resolutions were 1.842×10^{-6} RIU and 1.667×10^{-6} RIU, respectively. The maximum FOM of this sensor was 333.744 RIU^{-1}, and the optimal SL was 0.104 cm. In addition, the resonance wavelengths of the sensor were obtained as ultra-high linearity of $R^2 = 0.99959$, which ensures a stable sensor performance. Finally, the double peak displacement is investigated, and the DPSS is introduced. The maximum DPSS is 55,700 nm/RIU. This sensor enhances the possibility of accurately detecting a wide range of analytes and has great potential in biosensing, especially for the detection and monitoring of drugs.

Acknowledgments

This work was jointly supported by the Heilongjiang Provincial Natural Science Foundation of China [JQ2023F001], National Natural Science Foundation of China [12304480], Local Universities Reformation and Development Personnel Training Supporting Project from Central Authorities, Natural Science Foundation of Heilongjiang Province [LH2021F007], China Postdoctoral Science Foundation funded project [2020M670881], City University of Hong Kong Strategic Research Grant (SRG) [7005505], as well as City University of Hong Kong Donation Research Grants [DON-RMG 9229021 and 9220061].

ORCID

Chao Liu https://orcid.org/0000-0001-6382-008X

References

1. W. Luo, X. Li, S. A. Abbasi, S. Zhu, H. P. Ho and W. Yuan, *Opt. Lasers Eng.* **166** (202) 107588.
2. F. Mumtaz, B. Zhang, M. Roman, L. G. Abbas, M. A. Ashraf and Y. Dai, *Measurement* **207** (2023) 112386.
3. W. Liu, C. Liu, J. Wang, J. Lv, Y. Lv, L. Yang and P. K. Chu, *Results Phys.* **47** (2023) 106365.
4. A. K. Mishra, S. K. Mishra and B. D. Gupta, *Opt. Commun.* **344** (2015) 86.
5. Y. Wang, Q. Huang, W. Zhu, M. Yang and E. Lewis, *Opt. Express* **26**(2) (2018) 1910.
6. D. Dupont, A. Johansson, S. Marchin, O. Rolet, S. Marchesseau and J. Leonil, *J. Agri. Food Chem.* **59**(15) (2011) 8375.
7. Q. Wang and B. Wang, *Opt. Laser Technol.* **107** (2018) 210.
8. Q. Wu, N. Li, Y. Wang, Y. Xu, S. Wei, J. Wu and X. Cui, *Biosens. Bioelectron.* **144** (2019) 111697.
9. M. N. Hossen, M. Ferdous, M. A. Khalek, S. Chakma, B. K. Paul and K. Ahmed, *Sens. Bio-Sens. Res.* **21** (2018) 1.
10. N. Luan and J. Yao, *IEEE Photon. J.* **9**(2) (2017) 1.
11. M. B. Hossain, M. S. Hossain, S. R. Islam, M. N. Sakib, K. Z. Islam, M. A. Hossain and G. H. Cho, *Results Phys.* **18** (2020) 103281.
12. Y. Zhiyong, G. Bai, C. Wang, C. Liu, Z. Gao and K. Li, *Results Phys.* **41** (2022) 105943.
13. R. Q. Mu, A. Saharia and Y. Ismail, *IEEE Sens. J.* **24**(3) (2023) 2697.
14. M. Yarien, Q. Song, Y. Sun and Z. Yan, *Chin. Opt. Lett.* **18**(10) (2020) 100601.
15. P. Russell, *Science* **299**(5605) (2003) 358.
16. A. A. S. Falah, W. R. Wong and F. R. M. Adikan, *Opt. Laser Technol.* **145** (2022) 107474.
17. Z. Chi, Y. Zhang and D. Liu, *Opt. Commun.* **285**(9) (2012) 2466.
18. G. An, S. Li, X. Yan, X. Zhang, Z. Yuan, H. Wang and Z. Han, *Plasmonics* **12** (2017) 465.
19. C. Liu, W. Su, F. Wang, X. Li, Q. Liu, H. Mu and B. Liu, *IEEE Photon. Technol. Lett.* **30**(16) (2018) 1471.
20. F. Wang, C. Liu, Z. Sun, T. Sun, B. Liu and P. K. Chu, *IEEE Photon. J.* **10**(4) (2018) 1.
21. M. R. Islam, A. N. M. Iftekher, M. S. Anzum, M. Rahman and S. Siraz, *IEEE Sens. J.* **22**(6) (2022) 5628.
22. M. R. Islam, A. N. M. Iftekher, M. E. Haque, S. Tasnim and R. R. Karim, *Optik* **299** (2024) 171617.
23. W. R. Rashmi, M. F. Etu and S. Abbas, Enhancing Wavelength Sensing Range of SPR-PCF Using Dual Peak Double Resonance: An LSPR Based Approach. Department of Electrical and Electronics Engineering (EEE), Islamic University of Technology (IUT), Board Bazar, Gazipur-1704, Bangladesh, 2023.
24. Y. Chen, X. Li, Z. Yin, L. Wang, Y. Geng and X. Hong, *Appl. Opt.* **56**(5) (2017) 1550.
25. A. A. Rifat, R. Ahmed, G. A. Mahdiraji and F. M. Adikan, *IEEE Sens. J.* **17**(9) (2017) 2776.
26. Y. Wang, S. Li, Y. Guo, S. Zhang and H. Li, *Infrared Phys. Technol.* **114** (2021) 103685.
27. B. Li, X. Yan, X. Zhang, F. Wang, S. Li, T. Suzuki and T. Cheng, *Opt. Exp.* **29**(9) (2021) 12930.

28. C. P. Liu, R. C. Wang, C. L. Kuo, Y. H. Liang and W. Y. Chen, *Recent Patents Nanotechnol.* **1**(1) (2007) 11.
29. A. K. Shakya and S. Singh, *Measurement* **188** (2022) 110513.
30. A. Hassani and M. Skorobogatiy, *JOSA B* **24**(6) (2007) 1423.
31. J. Lv, H. Fu, C. Hu, Z. Yi, L. Yang, Y. Zeng and C. Liu, *Results Phys.* **40** (2022) 105876.
32. W. Liu, C. Hu, L. Zhou, Z. Yi, C. Liu, J. Lv and P. K. Chu, *J. Mod. Opt.* **67**(20) (2020) 1545.
33. W. Liu, C. Hu, L. Zhou, Z. Yi, C. Liu, J. Lv and P. K. Chu, *Phys. E, Low-Dimensional Syst. Nanostruct.* **138** (2022) 115106.
34. W. Liu, Y. Shi, Z. Yi, C. Liu, F. Wang, X. Li and P. K. Chu, *Opt. Exp.* **29**(25) (2021) 40734.
35. M. R. Islam, A. N. M. Iftekher, K. R. Hasan, M. J. Nayen, S. B. Islam, R. Islam and Z. Tasnim, *Appl. Phys. A* **127** (2021) 1.
36. M. R. Islam, A. N. M. Iftekhar, A. A. Hassan, S. Zaman and M. A. Hosain, *Appl. Phys. A* **129**(8) (2023) 571.